



Parallel Session IXa, June 1, Thursday

L37

COMBINED ANALYSIS OF CrAIN ENRICHED WITH Ta MAGNETRON SPUTTERED ON WC-Co SUBSTRATE

Martin Kusý¹, Patrik Šulháněk¹, Marian Haršáni² a Ivona Černičková¹

¹Institute of materials, Faculty of Materials Science and Technology in Trnava, Slovak University of Technology in Bratislava

²STATON, s.r.o., Sadová 1148, 038 53 Turany

In this study the combined analysis comprising of structure, texture, microstructure and stress analysis was applied to CrAIN thin coating enriched with Ta magnetron sputtered on WC-Co substrate. The analysis was carried out using the MAUD program following the concepts introduced in book entitled Combined analysis of Daniel Chateigner.

Experimental material was prepared by tilted co-deposition magnetron sputtering from CrAl and Ta targets on sintered WC-Co substrate which was maintained at 200°C. The pressure was held at 0.40 Pa.

PANalytical Empyrean diffractometer equipped with ChiPhi stage and characteristic Fe filtered Co radiation in

point focus was used for measurement. Primary arm contained polycapillary optic with cross slits while the secondary arm was equipped with 0.27 rad parallel plate collimator and proportional Xe detector. The Chi increment was 5° in the range from 0 to 80° and Phi increment at each Chi was 30° in the range from 0 to 360°. In total 204 diffraction patterns were collected in the 2theta range from 30 to 148°. The instrument broadening was determined by measuring NIST LaB6 660c position and profile standard in an entire angular range.

The coating structure model was build based on results from scanning electron microscopy (Fig. 1). The coating

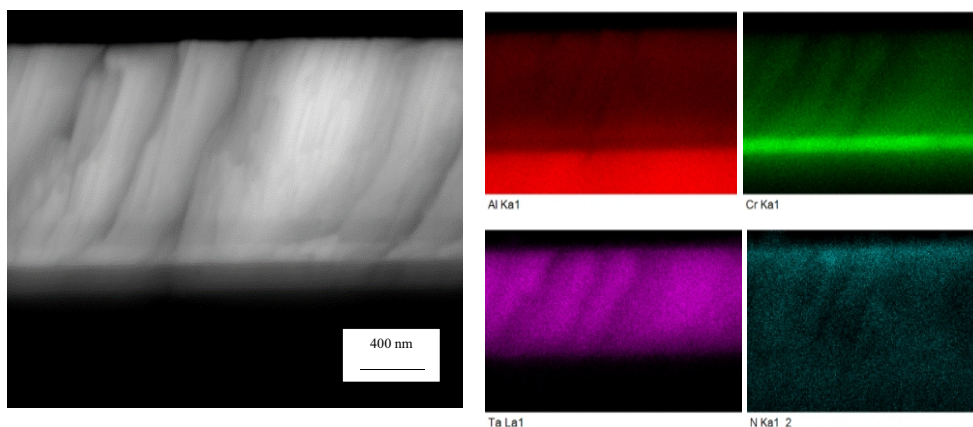


Figure 1. Microstructure and EDX map of the transversal coating fracture

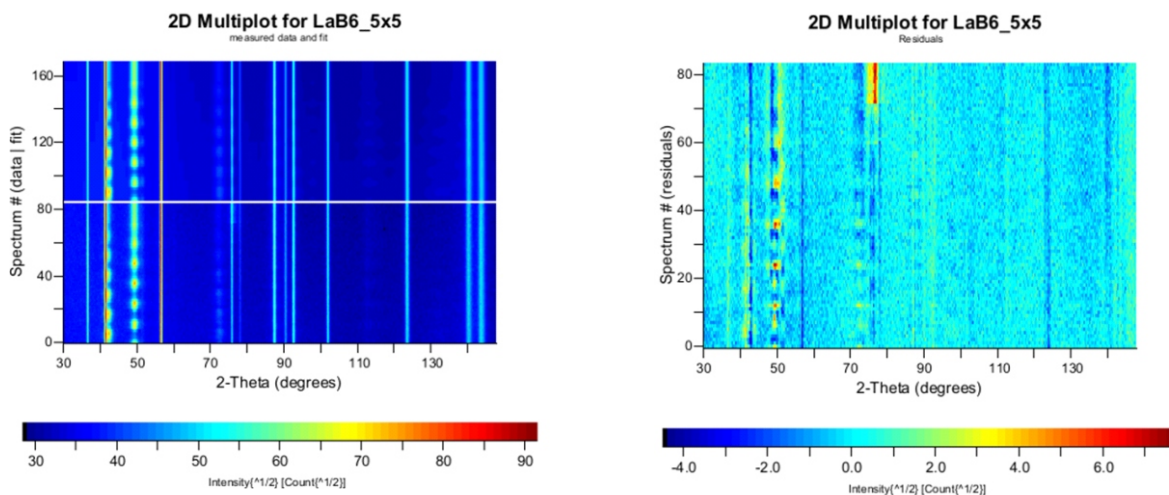


Figure 2. 2D plot of the diffraction patterns for Chi range from 0 to 30° with 2D difference plot

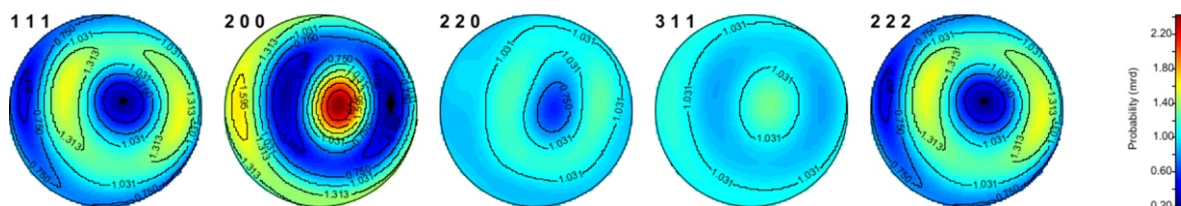


Fig. 3. Pole figures of the CrAlTaN phase

thickness was determined at approximately 1 μm with thin Cr adhesion layer at an approximate thickness of 200 nm. Chemical composition from EDX measurement revealed 12 at. % of Al, 16 at. % of Cr, 21 at. % of Ta and 49 at. % of N.

The layer model built in the MAUD program copied results from microstructural observations. WC-Co substrate model was determined separately from the identical XRD measurement of the substrate. Refined data were taken as constraints at the beginning of the refinement and represented the substrate layer. On top, adhesion Cr coating was modelled followed with the uppermost layer of CrAlTaN with corresponding atomic concentrations.

The quality of the final refinement stage achieved R_{wp} of 5.02 %. Example of the fit is provided in 2D and 2D resid-

ual image (Fig. 2). The final thickness of the coating was determined to 950 nm and adhesive Cr coating thickness 150 nm. The texture of the CrAlTaN described by Harmonics with -1 symmetry is represented by pole figures in Fig. 3. Crystallite size and microstrain were described using an anisotropic Popa model.

1. Lutterotti, L.; Matthies, S.; Wenk, H.R. MAUD (Material Analysis Using Diffraction): A user friendly Java program for Rietveld texture analysis and more. In Proceedings of the 12th International Conference on Textures of Materials (ICOTOM-12), McGill University Montreal, Montréal, QC, Canada, 9–13 August 1999; pp. 1599–1604. Available online: <http://hdl.handle.net/11572/57067> (accessed on 28 July 2021).
2. Chateigner, D.: Combined Analysis, Wiley, 2010

L38

MIKROSTRUKTURNÍ A ELEKTRICKÉ VLASTNOSTI ROTAČNĚ KOVANÉ MĚDI

Kopeček J.¹, Kmječ T.¹, Veřtát P.¹, Šimek D.¹, Ahmed U.¹, Duchoň J.¹, Klementová M.¹, Bajtošová L.², Kunčická L.³, Kocich R.³

¹FZU – Institute of Physics of the Czech Academy of Sciences, Praha

²Faculty of Mathematics and Physics, Charles University, Prague

³Faculty of Materials Science and Technology, VŠB–Technical University of Ostrava, Ostrava-Poruba

Měď vyniká výtečnou elektrickou vodivostí, ale její mechanické vlastnosti nejsou valné [1]. Když jsou pak zlepšeny, například příměsemi, dochází k rapidnímu snížení vodivosti, protože příměsové atomy, či částice, které je obsahují, rozptylují vodivostní elektrony. Vcelku překvapivou metodou řešení dilematu preferovat vyšší vodivost či mechanické vlastnosti se ukázaly být některé metody značné plastické deformace, které vytvářejí velké množství nanodvojčat [2]. V takto připravených vzorcích byla pozorována vyšší vodivost než v konvenčně žíhané mědi. Předpokládáme, že dvojčatové hranice, jako příklad speciálních hranic s velmi malou přebytečnou energií vrstevné poruchy, působí jako kanály vedoucí elektrický proud téměř bezrozptylově. Samozřejmě jiné poruchy, jako jsou obecné hranice zrn nebo dislokace elektrony rozptylují a zvyšují elektrický odpor, což vede k ohřevu materiálu a degradaci mechanických vlastností.

I po téměř dvaceti letech je koncept tvorby velkého množství nanodvojčat stále živý a dále rozpracováván pro různé materiály [3]. V naší práci jsme použili komerčně

čistou měď pro elektrické aplikace, která byla rotačně kována (RS) při teplotě kapalného dusíku v zařízení Komafu S600, při využití zkušeností členů týmu s metodikou RS [4-6]. Výchozí průměr tyčí byl 50 mm a redukovány byly na průměry 20 až 10 mm. Vykované tyče byly dále žíhány a všechny stavy byly standardně zkoumány pomocí SEM (Tescan FERA 3), EDS a EBSD (EDAX Octane super 60 mm² a Digiview IV), TEM (Jeol JEOL 2000 FX) a XRD (PANalytical X'Pert PRO).

Potvrdili jsme, že rotační kování vytváří silnou texturu ve směrech 100 a 111 v ose kování. Zrna jsou v materiálu velmi silně protažena ve směru osy tyče. Po žíhání tato mikrostruktura masivně rekrystalizuje, přesto však je vodivost ve všech případech vyšší než v konvenčně žíhané mědi pro elektrické aplikace. Tento výsledek je překvapivý, zejména s ohledem na relativně nízké množství dvojčat pozorovaných pomocí TEM. Prozatím předpokládáme, že pozorování poruch krystalové mříže je ovlivněno schopností mědi relaxovat i v nízkých teplotách [7].



1. J. R. Davies (Ed), ASM Specialty Handbook, Copper and Copper Alloys, Materials Park, ASM International, 2001.
2. L. Lu, Y.F. Shen, X.H. Chen, L.H. Qian, K. Lu, Ultrahigh strength and high electrical conductivity in copper, *Science*, 304 (2004), 422-426.
3. X. Ke, J. Ye, Z. Pan, J. Geng, M.F. Besser, D. Qu, A. Caro, J. Marian, R.T. Ott, Y.M. Wang, F. Sansoz, Ideal maximum strengths and defect-induced softening in nanocrystalline-nanotwinned metals, *Nature Materials*, 18 (2019), 1207-1214.
4. R. Kocich, L. Kunčická, A. Macháčková, M. Šofer, Improvement of mechanical and electrical properties of rotary swaged Al-Cu clad composites, *Mater. Design*, 123 (2017), 137-146.
5. P. Strunz, L. Kunčická, P. Beran, R. Kocich, Ch. Hervochoes, Correlating Microstrain and Activated Slip Sys-

- tems with Mechanical Properties within Rotary Swaged WNiCo Pseudoalloy, *Materials*, 13(2020), 208.
6. D. Canelo-Yubero, R. Kocich, J. Šaroun, P. Strunz, Residual Stress Distribution in a Copper-Aluminum Multifilament Composite Fabricated by Rotary Swaging, *Materials*, 16 (2023), 2102.
7. Král P., Staněk J., Kunčická L., Seitl F., Petrich L., Schmidt V., Beneš V., Sklenička V.: Microstructure changes in HPT-processed copper occurring at room temperature. *Mater. Character.* 151 (2019) 602-611.

Děkujeme projektu GA ČR 22-11949S a projektům MŠMT CzechNanoLab (LM2023051) a SOLID21 (CZ.02.1.01/0.0/0.0/16_019/0000760) za podporu.

L39

SMALL-ANGLE X-RAY SCATTERING STUDY OF LAMELLAE IN METASTABLE TITANIUM ALLOYS

J. Šmilauerová¹, P. Harcuba¹, J. Stráská¹, J. Stráský¹, M. Janeček¹, V. Holý²

¹*Department of Physics of Materials, Faculty of Mathematics and Physics, Charles University, Ke Karlovu 5, 121 16 Prague, Czech Republic*

²*Department of Condensed Matter Physics, Faculty of Mathematics and Physics, Charles University, Ke Karlovu 5, 121 16 Prague, Czech Republic*
jana.smilauerova@matfyz.cuni.cz

Metastable α -Ti alloys contain a sufficient amount of so-called β -stabilizing elements to prevent the formation of the low-temperature β phase (hcp) in the high-temperature α matrix (bcc) during quenching. After quenching, the β phase remains in a thermodynamically metastable state and, when annealed, it can decompose into other phases and complex phase transformations can be observed [1].

Quenched metastable α -Ti alloys often contain particles of the metastable β phase (hexagonal or trigonal lattice). These particles form by a diffusionless displacive transformation and have a size of several nm [2]. During annealing at lower temperatures, β particles evolve by a diffusion-assisted process and their size increases to several tens of nm

[3, 4]. When a metastable α -Ti alloy is aged at higher temperatures, or for a longer time, precipitates of the thermodynamically stable β phase start to nucleate either in the direct proximity of α particles, or, in their absence, directly from the α matrix [5, 1]. β particles have a lamellar shape and the crystallographic orientation between α and β is given by the Burgers orientation relationship [6]. However, the spatial orientation of the lamellae (i.e. the orientation of their habit plane) has been under much discussion. While some research identified the habit plane as (111) [7, 8], other studies reported the habit plane (11 11 13) [9].

In the present research, we used small-angle X-ray scattering (SAXS) to investigate the spatial orientation of

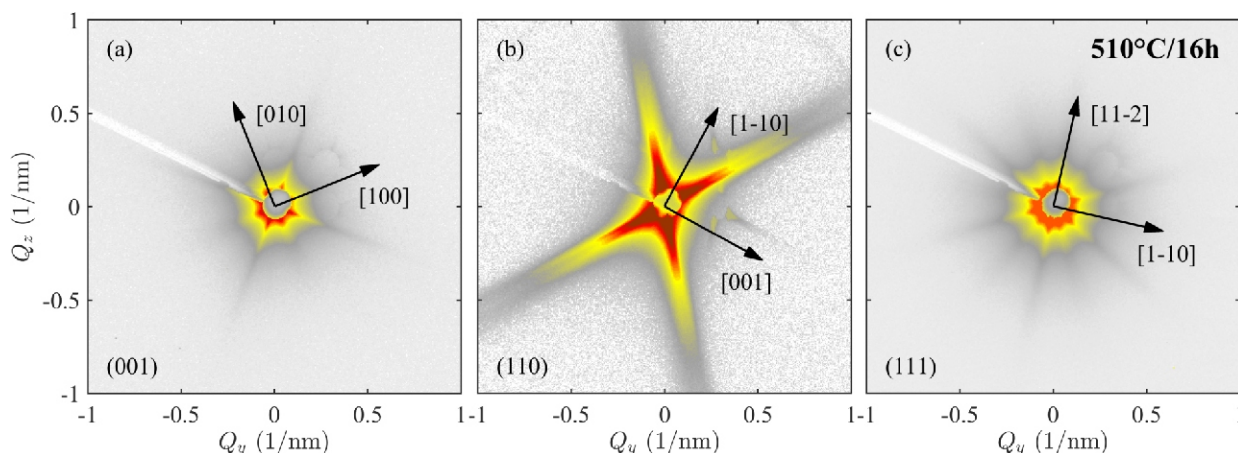


Figure 1. An example of measured SAXS patterns; sample aged at 510 °C for 16 h. The plane of the β matrix perpendicular to the primary beam is given in the bottom left corner of each panel.

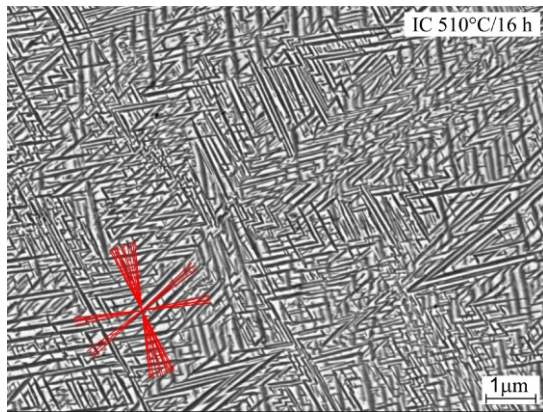


Figure 2. SEM micrograph (back-scattered electron contrast) of the sample aged at 510 °C for 16 h. lamellae are observed as darker regions in a lighter matrix. The red lines indicate the apparent directions of the lamellae resulting from the fit of SAXS data.

lamellae with respect to the parent phase in a metastable α -Ti alloy (Timetal LCB). Single crystals produced by the floating zone technique were used [10]. Consequently, the SAXS patterns represented a single grain, which allowed us to extract more complex information than if the scattering signal was averaged over many grain orientations. Different alloy conditions were prepared by annealing at selected temperatures below and above the solvus, which is approximately 500 °C for the Timetal LCB alloy [11]. More information on the annealing schemes can be found in [12].

Figure 1 shows an example of SAXS patterns measured for three orientations of the sample. Each sample was tilted to orient the planes (001), (110) and (111) perpendicular to the primary beam, see panels (a), (b) and (c) in Fig. 1, respectively. Note that the symmetry of the SAXS patterns depends on the sample orientation: four-, two- and six-fold symmetry is observed for the orientations (001), (110) and (111), respectively. Figure 2 shows an SEM image of the sample aged at 510 °C for 16 h.

The SAXS data were fitted by a model which simplified the shape of an lamella to a triaxial ellipsoid. We assumed that all lamellae are similar, i.e. their axes ratios are constant, and that the size distribution of particles follows the Gamma distribution. From the fit, we obtained the dependence of the dimensions of lamellae on the aging condition and we determined that the habit plane is close but not equal to (111). The slight deviation of the habit plane from (111) is confirmed by SEM, in which fans of similar apparent α directions can be observed; the apparent α directions resulting from the fit are represented by the red lines (Fig. 2). If the habit plane of the lamellae was exactly (111), the number of apparent directions would be reduced to only four, as there are four crystallographically equivalent (111) planes.

A Monte Carlo simulation of an SEM image was constructed using the values resulting from the fit, see Fig. 3. The comparison of figures 2 and 3 shows a good agreement between the real and simulated microstructures.

1. G. Lutjering & J. C. Williams, Titanium, 2nd ed., Berlin: Springer, 2007.
2. D. De Fontaine, Metall. Trans. A, 19, (1988), 169.

Figure 3. Monte Carlo simulation of an SEM image of α lamellae using the orientations and sizes fitted for the 510 °C/16 h sample.

3. J. Šmilauerová, P. Harcuba, D. Kriegner, M. Janeček and V. Holý, Acta Mater., 100, (2015), 126.
4. P. Zháňal, P. Harcuba, M. Hájek, B. Smola, J. Stráský, J. Šmilauerová, J. Veselý and M. Janeček, J. Mater. Sci., 53, (2018), 837.
5. T. Li, D. Kent, G. Sha, L. T. Stephenson, A. Ceguerra, S. P. Ringer, M. S. Dargusch and J. M. Cairney, Acta Mater., 106, (2016), 353.
6. W. G. Burgers, Physica, 1, (1934), 561.
7. Q. Guo, Q. Wang, X. L. Han, D. L. Sun, X. Wang and G. H. Wu, Micron, 41, (2010), 565.
8. T. Furuhashi, T. Makino, Y. Idei, H. Ishigaki, A. Takada and T. Maki, Mater. Trans. JIM, 39, 1998, 31.
9. R. Shi, N. Ma and Y. Wang, Acta Mater., 60, (2012), 4172.
10. J. Šmilauerová, J. Pospíšil, P. Harcuba, V. Holý and M. Janeček, J. Cryst. Growth, 405, (2014), 92.
11. P. Harcuba, J. Šmilauerová, M. Hájek, P. Zháňal and J. Čapek, in Proceedings of the 13th World Conference on Titanium, (2016), 437.
12. J. Šmilauerová, P. Harcuba, J. Stráská, J. Stráský, M. Janeček, J. Pospíšil, J. Ilavský and V. Holý, Mater. Charact., 196, (2023), 112615.

This work was supported by a joint project of the Czech Science Foundation (GACR) project no. 22-21151K and the Austrian Science Fund (FWF) project no. I5818-N. Single crystal growth was performed in MGML (<http://mgml.eu/>), which is supported by the Czech Research Infrastructures program (project No. LM2018096). This research used resources of the Advanced Photon Source, an Office of Science User Facility operated for the U.S. Department of Energy (DOE) by Argonne National Laboratory, supported by the U.S. DOE under Contract No. DE-AC02-06CH11357. National Science Foundation (NSF) ChemMatCARS Sector 15 is supported by the Divisions of Chemistry (CHE) and Materials Research (DMR), NFS, under Grant No. NSF/CHE-1834750.



L40

THERMALLY INDUCED RELAXATION OF CREEP INDUCED ANISOTROPY

D. Yudina¹, M. Marsilius², P. Sovák¹, J. Bednarčík^{1,3}

¹Institute of Physics, Faculty of Science, P.J. Šafárik University in Košice, Park Angelinum 9, 041 54 Košice, Slovakia

²VACUUMSCHMELZE GmbH & Co. KG, Hanau, Germany

³Institute of Experimental Physics, Slovak Academy of Sciences, Watsonova 45, 04001 Košice, Slovakia
jozef.bednarcik@upjs.sk

This work is focused on thermally induced relaxation of creep induced anisotropy (CIA) in the FeCuNbSiB nanocrystalline alloy [1]. The various extents of CIA were induced by stress annealing under applying tensile loads up to 480 MPa. Structural changes induced by annealing under uniaxial tensile deformation were investigated using synchrotron X-ray diffraction (XRD). It was shown that Fe₃Si nanocrystalline grains growing in the tensile direction have a higher value of the lattice spacing. An opposite behaviour is seen in transversal direction. The difference between the value of the lattice strain determined in the longitudinal and transverse directions is proportional to the magnitude of the tensile stress applied and represents a quantitative parameter determining the degree of creep induced anisotropy (CIA). Strain pole figure (SPF) measurements provide evidence that the CIA is uniaxial, and its main axis is aligned along tensile direction. Quantitative comparison of the SPFs shows that the strain partitioning among different Bragg reflections is not even and {400} family of planes exhibits the highest magnitude of the CIA. Furthermore, it was found that the magnitude of the CIA for a given set of Bragg reflections {hkl} is inversely proportional to its Young's modulus E_{hkl} [2].

XRD measurements presented in this work were performed at the P02.1 beamline of the 3rd generation synchrotron radiation source PETRA III at DESY (Hamburg, Germany) [3]. Figure 1 shows typical transmission geometry of XRD experiment at the P02.1 beamline. The incident X-ray beam with photon energy of 59.84 keV ($\lambda = 0.02072$ nm) was set to a cross-section of $0.5 \times 0.5 \text{ mm}^2$. About 2 cm long piece of a ribbon specimen was aligned with respect to

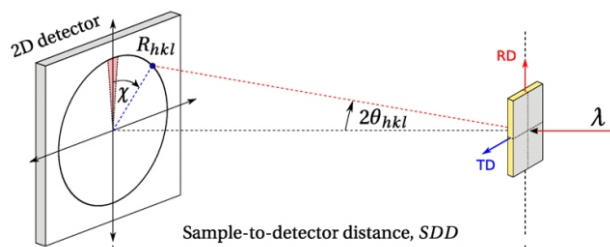


Figure 1. Typical arrangement of the in-situ XRD experiment performed in transmission (Debye-Scherrer) geometry at the P02.1 beamline. RD and TD refer to the rolling (tensile) and transversal directions, respectively. The sample was attached to the heater of the Linkam THMS 600 hot stage, so it was kept at desired temperature T_a .

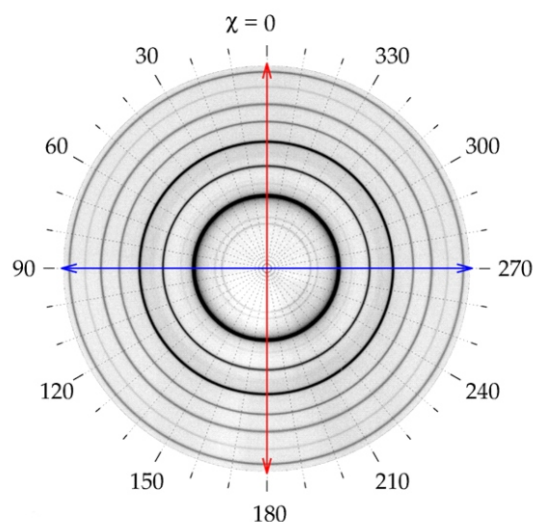


Figure 2. 2D XRD pattern of a sample prepared with a maximum value of tensile stress 482 MPa.

the incoming beam with tensile direction (RD) being perpendicular to the incident photon beam.

Each time a fresh specimen with a creep induced anisotropy was put inside a Linkam hot stage THMS 600. Temperature profile during *in-situ* XRD experiment consisted of two segments: i) constant rate heating at a 10 K/min up to desired temperature T_a followed by ii) isothermal annealing at T_a for up to 5 h. Exposure time per single 2D XRD pattern was set to 20 s. Scattered photons were collected using a 2D detector Perkin Elmer 1621 (2048×2048 pixels, pixel size $0.2 \times 0.2 \text{ mm}^2$) positioned 654.5 mm downstream from the sample.

Figure 2 shows a typical raw 2D XRD pattern as acquired with 2D detector PE1621. Series of concentric rings are due to presence of cubic Fe₃Si phase. The raw 2D XRD pattern was integrated with respect to the azimuth angle (caking procedure with $\Delta\chi = 2^\circ$) using pyFAI [4]. Such operation yielded 180 1D diffraction profiles $I(q)$ for azimuth angles χ (Figure 3). In other words, the raw diffraction pattern represented in the polar coordinate system (Figure 2) was transformed to the Cartesian coordinate system (Figure 3). The reason for doing such a transformation is to make data analysis more efficient. The presence of the residual strain in the sample prepared with a maximum value of tensile stress (482 MPa) is readily seen in the Cartesian coordinate system (Figure 3) as a wavy behaviour of the Bragg peak position with varying azimuth angle χ . This

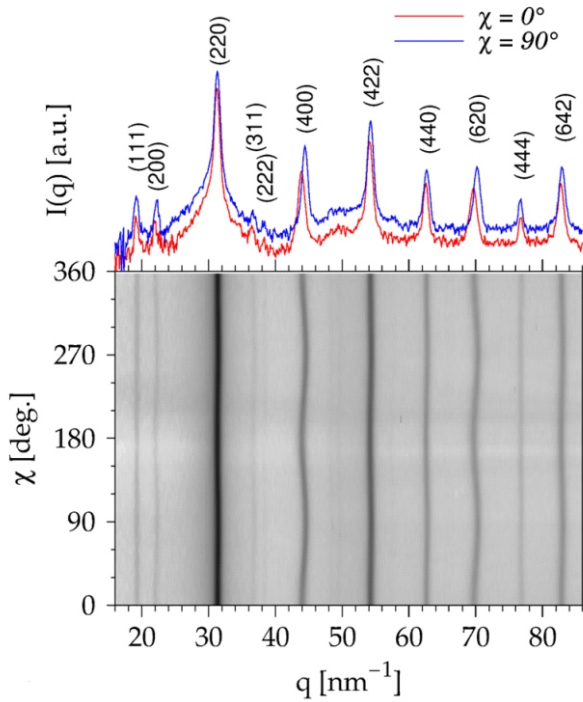


Figure 3. The image from Fig.2 after azimuthal integration using a pyFAI. Above 2D map selected intensity profiles corresponding to azimuth angles $\chi = 0^\circ$ (RD) and 90° (TD) are depicted. Bragg peaks corresponding to cubic Fe_3Si phase are labelled with Miller indices.

also means that the Bragg peaks appearing in the polar co-ordination system (Figure 2) as concentric rings are indeed ellipses. It is also important to note that the extent of distortion varies among different Bragg reflections. The lattice strain associated with a set of crystallographic planes $\{hkl\}$ can be defined as

$$\varepsilon_{hkl}(\chi) = \frac{q_{hkl}^0}{q_{hkl}(\chi)} - 1, \quad (1)$$

where q_{hkl}^0 is a reference value of the Bragg peak position and $q_{hkl}(\chi)$ is a peak position at given azimuth angle χ . There are several ways how to get a reference value. One could retrieve its value from a measurement on the sample annealed with the lowest value of tensile stress, i.e., 14 MPa. Another way is to use the data itself and calculate reference value from the so called zero stress azimuth directions [5,6] which are obtained by solving equation

$$3\cos^2(\chi) - 1 = 0. \quad (2)$$

In this work we used a later method. Figure 4 shows comparison of strain curves calculated according to equation (1) for different level of stress levels. The sample annealed under stress of 14 MPa shows no presence of CIA, which is indicated by the constant (zero) value of ε curve. With increasing tensile stress magnitude of the CIA increases as manifested by widening the gap between the maximum ($\chi = 0^\circ$) and minimum ($\chi = 90^\circ$) of strain curve (see Figure 4). Variation of ε with respect to the azimuth angle can be expressed by following equation

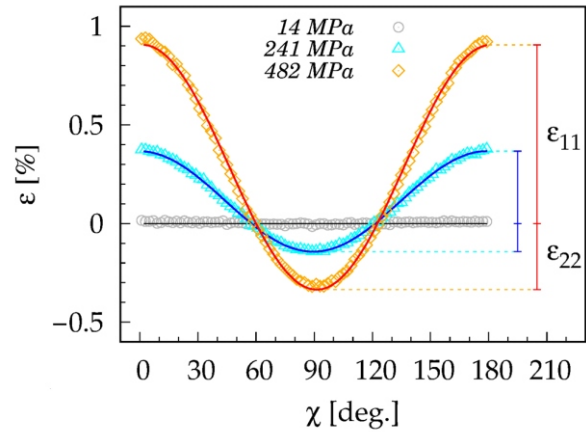


Figure 4. Comparison of lattice strains corresponding to samples annealed at different levels of tensile stress (14, 241 and 482MPa). Open signs refer to experimental measurements whereas solid lines represent fits to the equation (3).

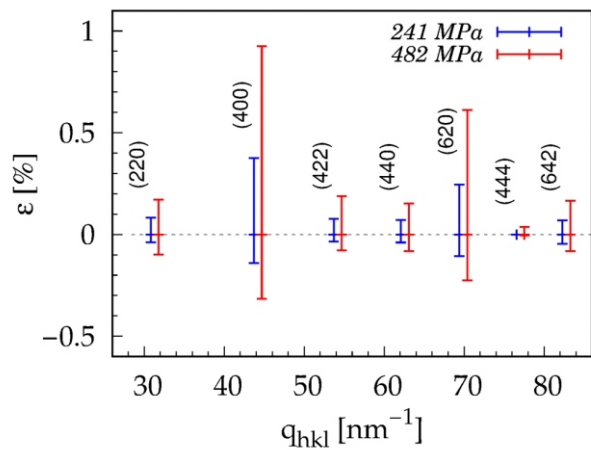


Figure 5. Comparison of strain partitioning among different Bragg reflections of Fe_3Si phase after applying tensile stress of 241 and 482 MPa.

$$\varepsilon(\chi) = \varepsilon_{11} \cos^2(\chi) + \varepsilon_{12} \cos(\chi)\sin(\chi) + \varepsilon_{22} \sin^2(\chi) \quad (3)$$

where ε_{11} is the longitudinal strain component, ε_{22} is the transversal strain component and ε_{12} is associated with the shear strain component. It should be noted here that these are three strain components associated with the plane defined by the incident X-ray photon beam being its normal vector. As can be seen from curves presented in Figure 4, equation (3) satisfactorily describes experimentally obtained strain data. Fitting experimental data of ε to the equation (3) numerical values of respective strain components were determined. In case a sample is well aligned with respect to the 2D detector the ε_{12} component becomes negligibly small.

Figure 5 shows partitioning of strain components among selected Bragg reflections of Fe_3Si phase as derived from 2D XRD data after applying tensile stress of 241 and 482 MPa. The data presented in the Figure 5 provide evidence that the strain partitioning among different Bragg reflections is not even and family of reflections $\{400\}$ shows the highest magnitude of CIA. The reason for such behav-

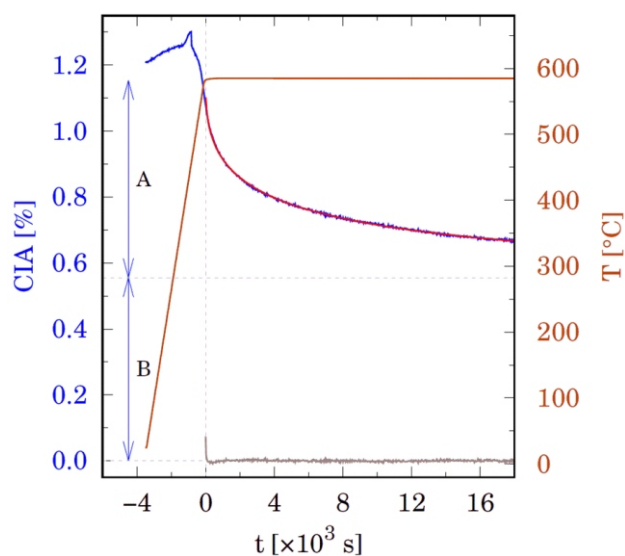


Figure 6. Creep-induced anisotropy behaviour for Bragg reflection (400) as a function of time and temperature, prepared with a maximum value of tensile stress 482 MPa. Solid red line shows the results of the fit using the exponential function. Vertical arrows refer to the actual values of amplitude and offset, *A* and *B*, respectively.

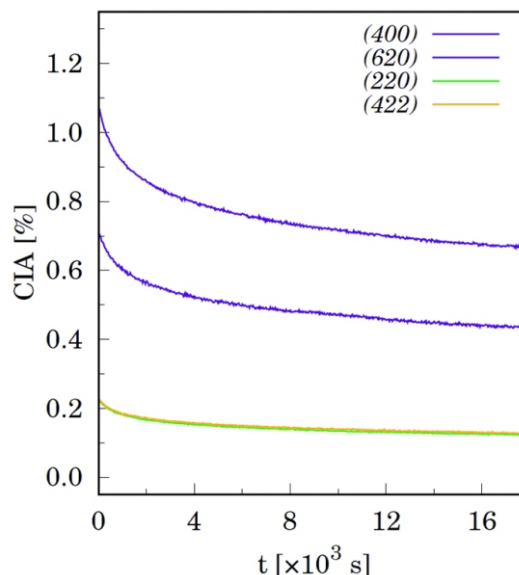


Figure 7. Temporal evolution dependence of creep-induced anisotropy for various Bragg reflection during isothermal annealing at 585 °C.

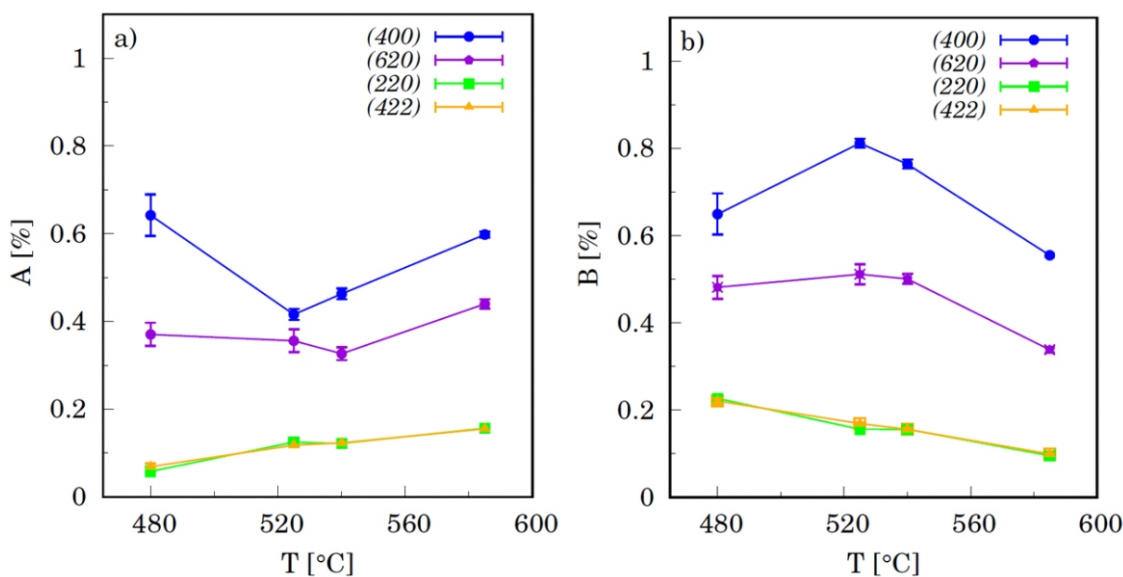


Figure 8. Variation of CIA amplitudes a) *A* and b) *B* as obtained by fitting experimental data to the equation (4). Each measurement started with a fresh sample prepared with a maximum value of tensile stress 482 MPa.

behaviour is because Young's moduli corresponding to respective Bragg reflections are having different magnitudes [7].

Figure 6 shows creep induced anisotropy (CIA) for Bragg reflection (400) as a function of time and temperature. The magnitude of CIA can be quantified as a sum of magnitudes of the longitudinal and transversal lattice strain, i.e., $|CIA| = |\epsilon_{11} + \epsilon_{22}|$. When heating a sample to the temperature of 585 °C, it can be seen that structural changes occur in the sample and a peak appears, which then completely disappears, and when the temperature reaches 585 °C, the CIA value decreases exponentially. The solid red line shown in Figure 6, well describing the measured experimental curve, is the results of fitting using exponential equation

$$|CIA| = A \exp(-kt^n) + B \tag{4}$$

where *A* is the amplitude, *t* is time, *B* is offset, parameters *k* is the decay parameter and *n* corresponds to the stretching exponent. Figure 7 shows CIA temporal evolution of CIA for various Bragg reflections during isothermal annealing at 585 °C. By fitting experimental data of the CIA curve to the equation (5) numerical values of respective amplitudes, offset, decay parameter and stretching exponent were determined.

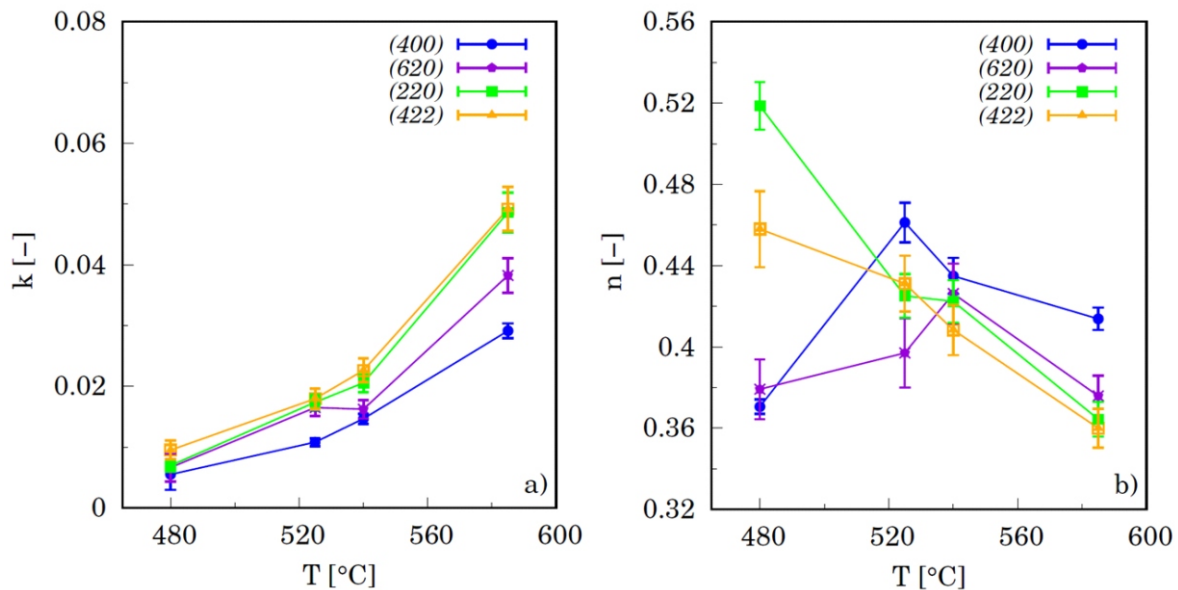


Figure 9. Variation of parameters a) k and b) n as obtained by fitting experimental data to the equation (4). Each measurement started with a fresh sample prepared with a maximum value of tensile stress 482 MPa.

Figures 8 and 9 show numerical results obtained from analysing temporal evolution of CIA during isothermal annealing at temperatures 480, 525, 540 and 585 °C.

Parameter B represent part of the CIA amplitude, which cannot be removed from specimen by isothermal annealing. On the other hand, A represents part of the CIA amplitude which can be annealed out by extending annealing time to infinity. Data suggest that Bragg reflections showing highest magnitude of CIA also show highest resistance to annealing effects. As can be seen from Figure 9a, the decay parameter k increases with increasing temperature. This implies faster removal of CIA at higher temperatures.

1. G. Herzer, V. Budinsky, C. Polak, *Journal of Physics: Conference Series*, **266**, (2011), 012010.
2. D. Yudina., M. Marsilius, J. Bednarcik, *J. Alloys and Comp.*, **123**, (2023), submitted for publication.

3. A.-C. Dippel, H.-P. Liermann, J. T. Delitz, P. Walter, H. Schulte-Schrepping, O. H. Seeck, H. Franz, *Journal of Synchrotron Radiation*, **22**, (2015), 675–687.
4. J. Kieffer, V. Valls, N. Blanc, C. Hennig, *Journal of Synchrotron Radiation*, **27**, (2020), 558–566.
5. J. Bednarcik, L. Y. Chen, X. D. Wang, J. Z. Jiang, H. Franz, *Metallurgical and Materials Transactions A*, **43**, (2012), 1558–1563.
6. N. Mattern, J. Bednarcik, S. Pauly, G. Wang, J. Das, J. Eckert, *Acta Materialia*, **57**, (2009), 4133–4139.
7. J.-M. Zhang, Y. Zhang, K.-W. Xu, V. Ji, *Journal of Physics and Chemistry of Solids*, **68**, (2007), 503–510.

This study was supported by the grant VEGA 1/0406/20. Parts of this research were carried out at the light source PETRA III (beamline P02.1) at DESY, a member of the Helmholtz Association (HGF). Tools for RNA and DNA structural description at dnatco.datmos.org